A consistent picture of TRPV1 activation emerges from molecular simulations and experiments

Marina A. Kasimova[1], Aysenur Yazici[2], Yevgen Yudin[2], Daniele Granata[1], Michael L. Klein[1], Tibor Rohacs[2], Vincenzo Carnevale[1]*

[1]*Institute for Computational Molecular Science, Temple University, Philadelphia, PA 19122*
[2]*Department of Pharmacology, Physiology and Neuroscience, Rutgers–New Jersey Medical School, Newark, NJ 07103*

*Email: vincenzo.carnevale@temple.edu

ABSTRACT

Although experimental structures of both the TRPV1 closed and open states are available, the conformational changes occurring in the pore domain and resulting in ionic conduction remain elusive. Here, we use bioinformatics analyses, molecular dynamics simulations and site-directed mutagenesis to shed light on this issue and suggest a possible molecular mechanism for TRPV1 activation. In light of our hypothesis, we re-examine the results of the previously published water accessibility and mutagenesis experiments, and analyze the newly available structures of TRP and other evolutionary related ion channels. Overall, we show that several independent lines of evidence corroborate our hypothesis, which highlights the rotation of a conserved asparagine toward the pore and the dehydration of hydrophobic cavities as key components of TRPV1 activation. Importantly, this molecular mechanism provides also a rationale for the coupling between the TRPV1 upper and lower gates.

INTRODUCTION

TRPV1 is a member of the transient receptor potential (TRP) family, which promotes non-selective cation current across cell membranes in response to heat, low pH, and inflammatory agents (1–3). Activation of this channel induces burning pain: the action potential triggered by TRPV1 in sensory ganglia and small sensory C-and Aδ fibers is transmitted through the second-order projection neurons in the spinal cord to the thalamus and specific higher order brain areas where it is perceived as pain (4, 5).

TRPV1 is a homotetramer with each subunit being composed of the transmembrane and cytoplasmic regions (6–8). The transmembrane region has six helical segments (S1 through S6); four of them (S1 through S4) constitute a domain structurally homologous to the voltage sensor domain of voltage-gated ion channels. The remaining two helices (S5 and S6) assemble into the pore domain. Cryo-EM structures of TRPV1 in different functional states have revealed key elements of its activation mechanism (6–8). For instance, it became apparent that TRPV1 has an upper gate at the level of the selectivity filter and a lower gate at the crossing of the S6 helical bundle. At room temperature binding of the agonist capsaicin between S4 and S5 promotes opening of the lower gate (7). The molecular mechanism of this conformational change has been in part clarified by mutagenesis experiments (8, 9): capsaicin forms a hydrogen bond with the S4-S5 linker and pulls it in the outward direction; as for voltage-gated ion channels, this motion relieves the constriction exerted by the linker on the S6 helical bundle.

However, the cryo-EM structure of the capsaicin-bound state is closed at cryogenic temperatures: both the selectivity filter and the lower gate are narrower than those of the open state (7), and in simulations they are dehydrated (10). Consistently, Jara-Oseguera et al. have shown that TRPV1 activation becomes increasingly less probable as temperature is decreased even when capsaicin is present in large concentrations (11). Thus, the capsaicin-bound state is closed at cryogenic temperatures and opens as temperature is increased with the mid-point of activation located approximately at 300 K.

We recently used molecular dynamics and free energy calculations to study the molecular mechanism of the closed-to-open transition in the capsaicin-bound state (10). Our major finding was that the conserved asparagine N676 adopts two alternative conformations in the open and closed states, projecting its side chain towards either the pore or four peripheral cavities located between the S6 helix and the S4-S5 linker, respectively. When TRPV1 is in the closed state, these cavities are connected to the intracellular solution and host several water molecules. Dehydration of peripheral cavities correlates with the rotation of N676 from these cavities toward the central pore of which N676 promotes hydration and thus permeability to ions (Fig. 1).

Here, we will briefly summarize our computational findings and discuss several lines of evidence in support of our hypothesis gathered from independent experimental investigations. We will discuss how these lend credibility to the rotation of N676 and the presence of peripheral cavities. We will then show how the suggested molecular

mechanism might be responsible for the observed coupling between the upper and lower gates.

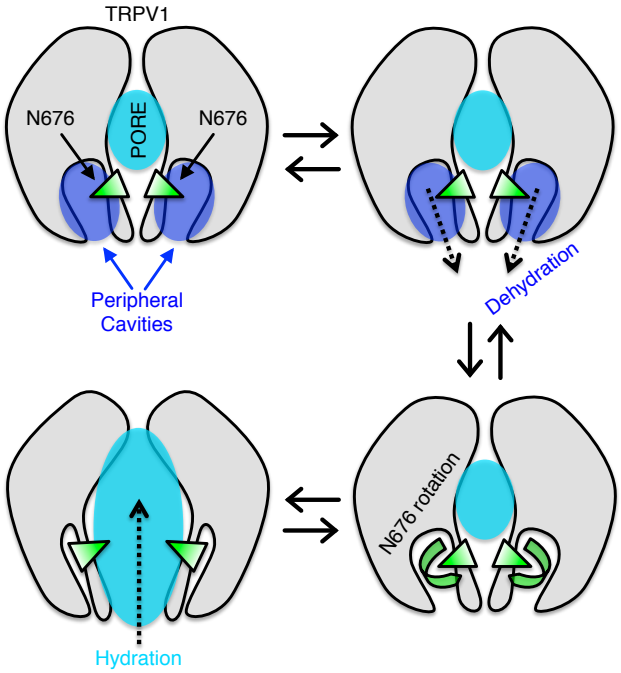

Figure 1: A possible molecular mechanism for TRPV1 activation (10). The channel is shown in grey; water in the pore and peripheral cavities in cyan and blue, respectively; the conserved asparagine N676 in green. In the capsaicin-bound closed state, the peripheral cavities host several water molecules, while the pore is partially dehydrated; N676 projects its side chain toward peripheral cavities. Upon application of an activating stimulus, the peripheral cavities dehydrate, an event that correlates with the rotation of N676 toward the pore. The presence of a hydrophilic side chain inside the pore promotes its hydration and hence permeability to ions.

RESULTS AND DISCUSSION

The π-bulge in the S6 helix is evolutionarily conserved across the TRP family

We start by recalling a remarkable feature of the capsaicin-bound structure (7): the presence of a π-helical segment between Y671 and N676 (Fig. 2A). α- and π-helices show an important difference: while in α-helices hydrogen bonds join main chain groups that are four residues apart (i-i+4), this spacing changes to five residues in π-helices (i-i+5). Therefore, the presence of a π-helical segment in a α-helix implies a mismatch in the pattern of hydrogen bonds, which results in unpaired carbonyl and amino groups. In practice, one residue does not participate in the network of hydrogen bonds and bulges out of the α-helix forming a so-called π-bulge (Fig. 2A). The π-bulge is mobile: the bulging residue can “reabsorb” by forming hydrogen bonds at the expense of a neighboring residue, which, as a result, bulges out of helix.

In one of our previous investigations we hypothesized, on the basis of the sole TRPV1 structure, that this structural motif is conserved across the entire family of TRP channels (12). To test this hypothesis, we analyzed patterns of correlations in a large multiple sequence alignment containing approximately 3000 distinct sequences of genes encoding for TRP channels. The presence of a π-helical segment changes the register of the downstream α-helix: it offsets by one position all the subsequent residues effectively imparting a rotation of 100 deg to the downstream α-helix (Fig. 2B). The change of the register results in a specific pattern of contacts between S6 and the neighboring S5. We detected this pattern in the multiple sequence alignment as strong correlations between S5 and S6 residues; importantly, these pairs of residues are in spatial proximity only with the "correct" register of S6, *i.e.* if the π-bulge is present (12). The conservation of this specific pattern of contacts between S5 and S6 across the entire TRP family suggests that the π-bulge is conserved as well.

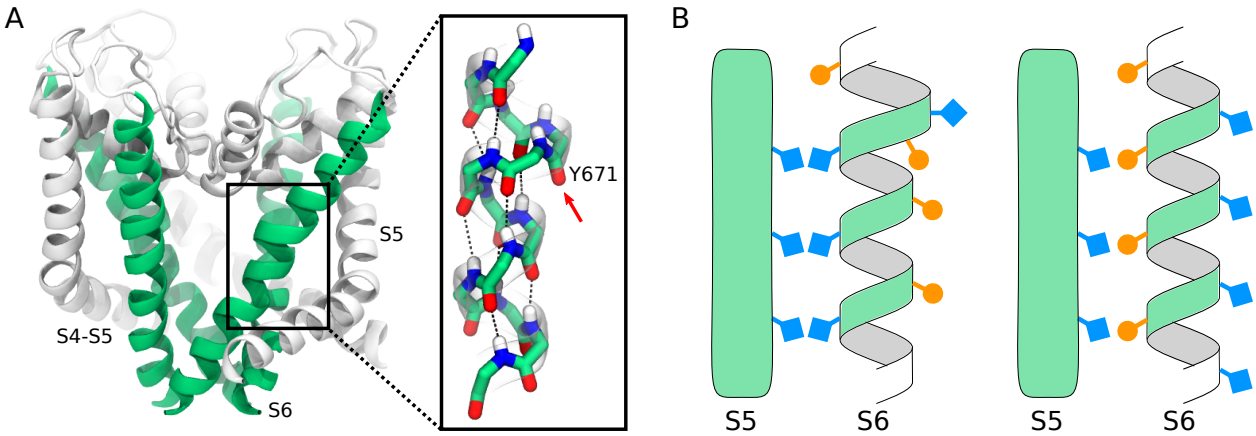

Figure 2: π-helical segment in the S6 helix of TRPV1. A. Cartoon representation of the TRPV1 pore domain (7). The S6 helices are colored in green, and the rest of the pore domain in white. The inset shows the π-helical segment and the π-bulge located on the Y671 residue (highlighted with an arrow). The atoms are colored by element type: C in green, N in blue, O in red, and H in white. B. Schematic representation of an α-helix (right) and an α-helix with a π-bulge (left). Note that the residues facing S5 in the α-helix are lining the pore when the π-bulge is introduced.

Since then several experimental structures of TRP channels have confirmed our hypothesis about the structural conservation of the π-bulge. The structures of TRPV1, TRPV6, TRPA1, TRPM4 and TRPP2 all show a π-helical segment in their S6 (6–8, 13–20).

The π-bulge causes conformational flexibility of neighboring residues

The multiple sequence alignment also highlighted the presence of a strictly conserved asparagine located in the vicinity of the π-bulge (N676 in TRPV1, Fig. 3A and B) (12). We hypothesize that the π-bulge endows this residue with conformational flexibility. Consistently, independent structures of different TRP channels (6–8, 13–25) show that the orientation of the conserved asparagine with respect to the pore can differ by as much as 180° between two structures (Fig. 3C). For instance, in the TRPP2 and TRPV2

structures this residue points toward the center of the pore or to the S4-S5 linker, respectively. In all the other TRP structures (TRPV1, TRPV5, TRPV6, TRPA1, TRPM4 and TRPM8) the conserved asparagine adopts intermediate orientations (Fig. 3C).

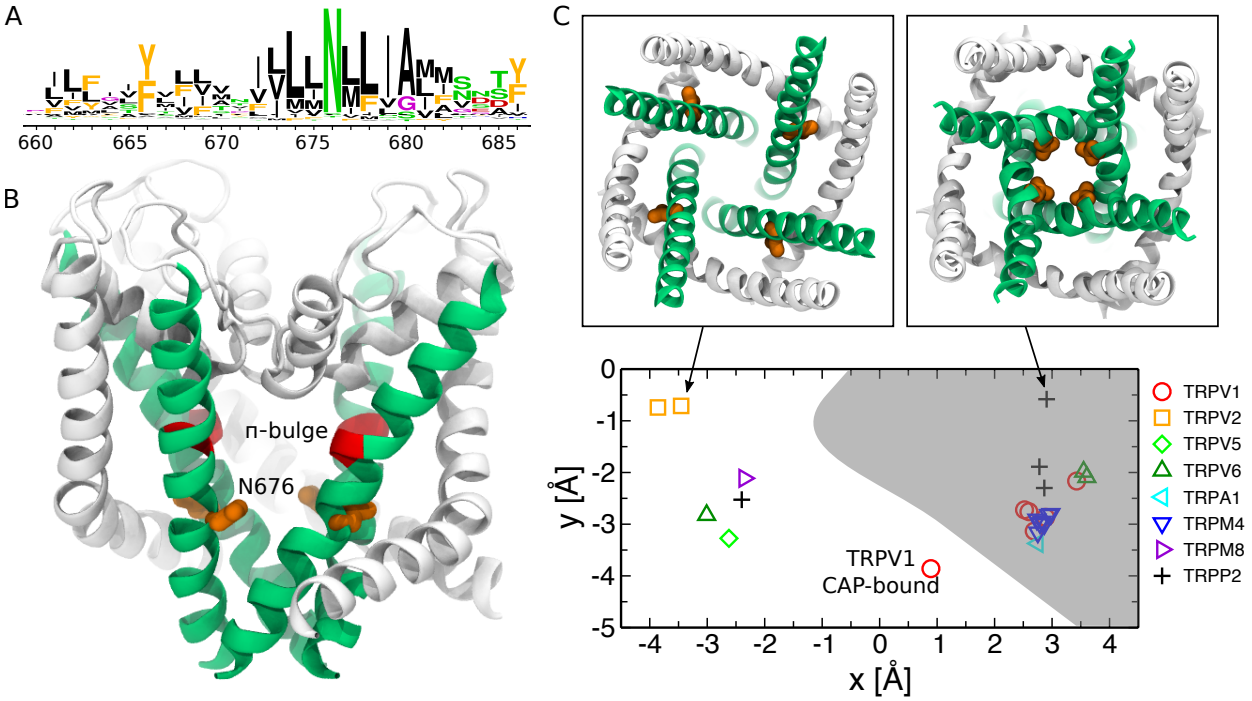

Figure 3: The conserved asparagine adopts two alternative conformations pointing either toward the pore or toward the S4-S5 linker. A. Multiple sequence alignment of the S6 helix across the TRP family (numbering based on the TRPV1 sequence) (12). B. Cartoon representation of the TRPV1 pore domain (7). The S6 helices are shown in green, and the rest of the pore domain in white. The π-bulge and the neighboring conserved asparagine are colored in red and orange, respectively. C. Orientation of the conserved asparagine with respect to the pore in different TRP structures (6–8, 13–25). The position of the asparagine side chain in the plane perpendicular to the pore axis is shown. X-axis is aligned with the vector connecting the Cα-atom of the asparagine and the center of the pore. The grey shaded area highlights the pore region. The two insets show the pore domains of TRPV2 (left) and TRPP2 (right): the conserved asparagine points toward the S4-S5 linker in TRPV2 and the center of the pore in TRPP2.

This structural heterogeneity is per se striking: evolutionary conservation points to functional relevance, yet the residue lacks a well-defined conformation; this immediately raises the question: is the role of N676 related to its flexibility? A very recent structural determination of the open and closed states of TRPV6 indicates that this is the case and fully supports the notion of a rotation in and out of the pore of several S6 residues (13). In particular, the structure with the asparagine facing the S4-S5 linker corresponds to a closed state, while that with the asparagine facing the pore to an open one. Such a conformational change can significantly affect the polarity of the pore surface and hence ionic transport. This effect is expected to be especially prominent when the rest of the pore is hydrophobic, as in the case of the TRP family (Fig. 3A).

Y671 motion affects gating at the selectivity filter and is coupled to N676 rotation

Is there any experimental evidence that the rotation of S6 residues underlies TRPV1 gating? Steinberg et al. recently showed that the gating correlates with a conformational change of Y671, a residue located on the π-bulge (26). To show this, a non-natural amino acid bearing a 7-hydroxycoumarin moiety was incorporated at position 671; the fluorescence of coumarin was then used as a local hydration reporter. It was found that, upon activation by capsaicin, the photon counts and optical fluctuations increase significantly, indicating a conformational transition of the side chain at position 671 and a change of its environment. In particular, and somewhat counterintuitively, the side chain at position 671 becomes less hydrated in the open state compared to the closed one (26).

Molecular dynamics simulations independently confirmed that, on passing from the closed to the open state, there is a significant decrease in the solvent accessible surface area of the side chain at position 671 (26): in the closed and open states, the fraction of the side chain surface accessible to water is 30% and 15%, respectively. Importantly, the same simulations are also able to explain why the solvent exposure of Y671 changes upon activation. The crux is that the conformational change of Y671 coupled to N676 rotation between the pore and peripheral cavities. In particular, a hydrogen bond between the N676 carboxamide and the I672 carbonyl oxygen stabilizes the π-bulge on I672 in the open state (Fig. 4A). By contrast, N676 points toward the peripheral cavity in the closed state and cannot donate any hydrogen bond to the main chain. As a consequence, the π-bulge is found preferentially on Y671 (Fig. 4A). The displacement of the π-bulge from I672 to Y671 causes a change of Y671 orientation with respect to the pore: it goes from being perpendicular to the pore axis in the open state to being parallel to it in the closed state (Fig. 4A and B). Finally, the pore helices shield Y671 from water more in perpendicular conformation than in the parallel one (Fig. 4B).

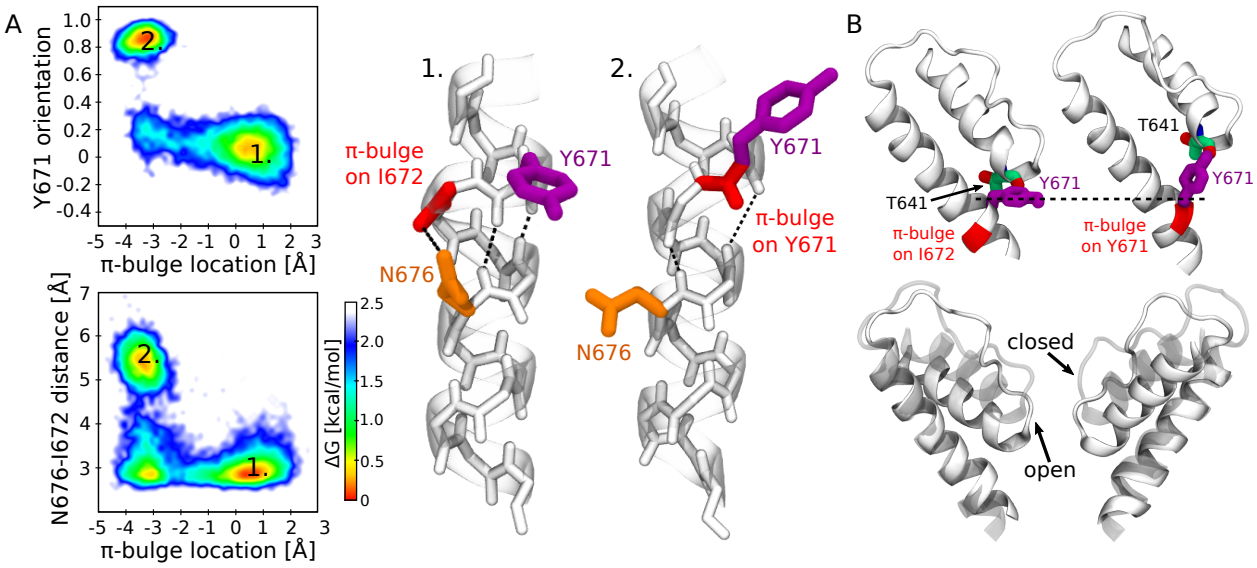

Figure 4: Two different conformations of the S6 helix in the TRPV1 closed and open states. A. Coupling between N676 and Y671. The top left panel shows Y671 orientation (the cosine of the angle between the Cα-Cγ vector and the pore axis) and the π-bulge position (the difference between the two distances: I672 carbonyl oxygen – N676 amine hydrogen and Y671 carbonyl oxygen – N676 amine hydrogen; positive values indicate the location of the π-bulge on I672, while negative ones indicate that the π-bulge is on Y671). Only two conformations are observed: open state (1), Y671 is perpendicular to the pore axis, and the π-bulge is on I672; closed state (2), Y671 is parallel to the pore axis, and the π-bulge is on Y671. The bottom left panel shows the distance between N676 carboxamide carbon and I672 carbonyl oxygen and the π-bulge position. The energetically most favorable conformations are: open state (1), a hydrogen bond between N676 carboxamide and I672 carbonyl oxygen is present, and the π-bulge is on I672; closed state (2), the hydrogen bond between N676 carboxamide and I672 carbonyl oxygen is absent, and the π-bulge is on Y671. The right panel shows the cartoon representations of the two conformations. Y672 is colored in purple, the π-bulge in red, and N676 in orange. The dashed lines show the network of hydrogen bonds. B. A change of Y671 orientation results in a displacement of the pore helix. The top panel shows the conformations of Y671 and of the adjacent pore helix in the open (left) and closed (right) states. The bottom panel shows the superposition between the pore helix in the open (solid) and closed (transparent) states.

The coupling between N676 and Y671 has another important implication. In our previous study we have shown N676 rotation correlates with hydration of the pore at the level of the lower gate (10). Interestingly, the change of Y671 orientation is potentially coupled to hydration of the other gate, *i.e.* the selectivity filter (Fig. 4B). In the conformation parallel to the pore axis, Y671 hydroxyl donates a hydrogen bond to T641 carbonyl located on the pore helix; this interaction displaces the pore helix toward the extracellular solution, a motion that results in the constriction of the selectivity filter (Fig. 4B). We hypothesize that this chain of events, involving N676, the π-bulge, Y671 and the pore helix is responsible for the observed coupling between the TRPV1 lower and upper gates.

Are the peripheral cavities are the missing piece of the puzzle?

The molecular mechanism suggested here agrees with the one emerging from the recently resolved TRPV6 structures (13) and complements it with a detailed description of the conformational changes involved in activation: the rotation of the conserved asparagine increases the hydrophilicity of the pore surface thereby promoting the hydration of this compartment. An interesting finding provided by the molecular dynamics simulations and not anticipated by these structures is the factor stabilizing the closed state, in which the asparagine is located outside the pore. In the TRPV1 closed state, our simulations have shown that N676 is accommodated inside a small hydrophobic cavity located between the S4-S5 linker and S6 and connected to the intracellular solution (10). This cavity, which we call peripheral in contrast to the central cavity in the ion conduction pathway, hosts several water molecules forming hydrogen bonds with N676 carboxamide. Importantly, the hydration of the peripheral cavity and the N676 rotation are correlated (10): when the peripheral cavity dehydrates, N676 rotates inside the pore. Based on this observation, we suggested that at, least for some stimuli, activation of TRPV1 is triggered by the dewetting of the peripheral cavities (10).

Is there any experimental evidence that supports the existence of these peripheral cavities? Overall, we found four independent observations, which can be retrospectively interpreted in light of this suggested molecular mechanism: (i) experiments probing S6 accessibility to intracellular solution (27), (ii) structural studies of the evolutionary related voltage-gated sodium and calcium channels (28–37), (iii) site-directed mutagenesis experiments targeting S6 and S4-S5 residues (38), some of which performed by us and presented in this study for the first time.

In a milestone paper by Salazar et al. (27), the authors probed the accessibility of the TRPV1 pore residues to the intracellular solution; they mutated, one by one, all the S6 residues to cysteine and assessed their accessibility to thiol-modifying reagents in the open and closed states. Their results showed that modification of D654-Y671 is more prominent in the open state than in the closed one, and that the modification of M682-G683 is state-independent. Interestingly, the rest of S6, namely the L681-I672 segment, showed different accessibility only when a bulky reagent was used; application of small reagents in the open or closed states in contrast resulted in a similar effect. Based on this data, the authors suggested the presence of lower and upper gates located at the level of L681 and Y671, respectively; both gates are open in the open state, while in the closed state the upper gate is closed and the lower gate is partially open (27). This elegant explanation, however, turned out to be inconsistent with the structural information subsequently obtained via cryo-EM on the apo state (6), in which both gates were found to be tightly constricted with a radius of ~ 1.0 Å, *i.e.* impermeable to any solute.

Can the presence of peripheral cavities solve this apparent contradiction? To answer this question, we characterized the accessibility of the TRPV1 pore residues in the open and two closed states, including capsaicin-bound closed and apo closed (Fig. 5). In agreement with Salazar et al., we found that all of the S6 residues are accessible to the intracellular solution in the open state. Moreover, we found that the same set of residues, namely the I672-G683 segment, is accessible in the closed state. Despite the constriction at the level of I679, the residues up to Y671 do interact with the intracellular solution. However, the interacting water molecules are not located in the pore, but rather in peripheral cavities. Therefore, one can easily resolve the contradiction between the water accessibility experiments (27) and the structural information (6) by considering that the S6 residues are accessible to the intracellular solution through the peripheral cavities.

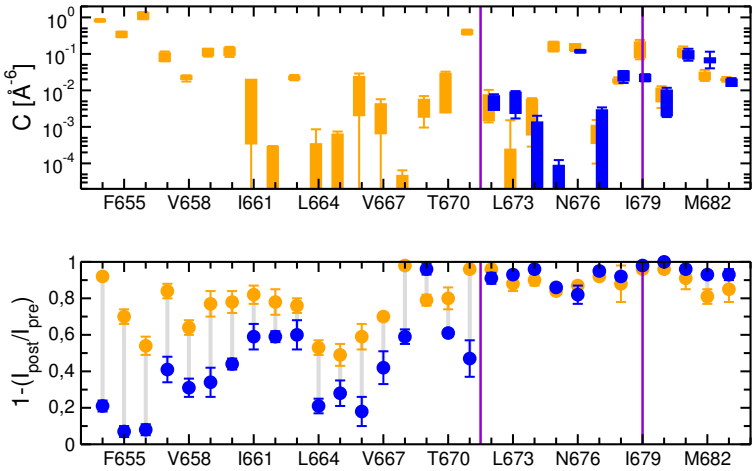

Figure 5: Accessibility of the S6 residues to the intracellular solution in the TRPV1 open (orange) and closed (blue) states. The top panel shows the computational results, while the bottom panel shows the experimental data extracted and digitalized from (27). In the simulations, water accessibility is calculated as the overlap between the atomic density of a given S6 residue and that of the intracellular water (the values shown correspond to a sum over all four channel subunits). The open state data corresponds to the results obtained for the capsaicin-bound open state (10); the closed state data corresponds to the results obtained for the capsaicin-bound closed state and the apo closed state (6, 10). The box plots report median and interquartile range with the whiskers representing the standard deviation. In the experiments, accessibility to the intracellular solution is measured as an effect on current after application of a thiol-modifying reagent. The purple lines highlight the position of Y671 (the hypothetical upper gate according to Salazar et al. (27)) and I679 (the lower gate).

The second piece of evidence in support of peripheral cavities comes from the structurally homologous and evolutionary related voltage-gated sodium and calcium channels (Nav and Cav). Also these two families show a conserved asparagine in the position corresponding to N676 (Fig. 6A). Mutagenesis of this residue into an aspartate affects dramatically the biophysical properties of the bacterial sodium channel NaChBac (39). Furthermore, the structures of Nav and Cav channels show that the conserved asparagine can adopt both the pore inward-facing (NavPas – all subunits, NavEel – one subunit out of four) and outward-facing conformations (Cav1.1 – all subunits, NavAb, NavRh, NavMs, NavEel – three subunits out of four) (Fig. 6B and C) (28–37). Do these channels have peripheral cavities? A recent high-resolution structure of the bacterial sodium channel NavMs shows the presence of four cavities, whose location coincide with that of peripheral cavities in TRPV1 (37). Moreover, similar to peripheral cavities, they host the side chain of the conserved asparagine and, importantly, few water molecules interacting with it.

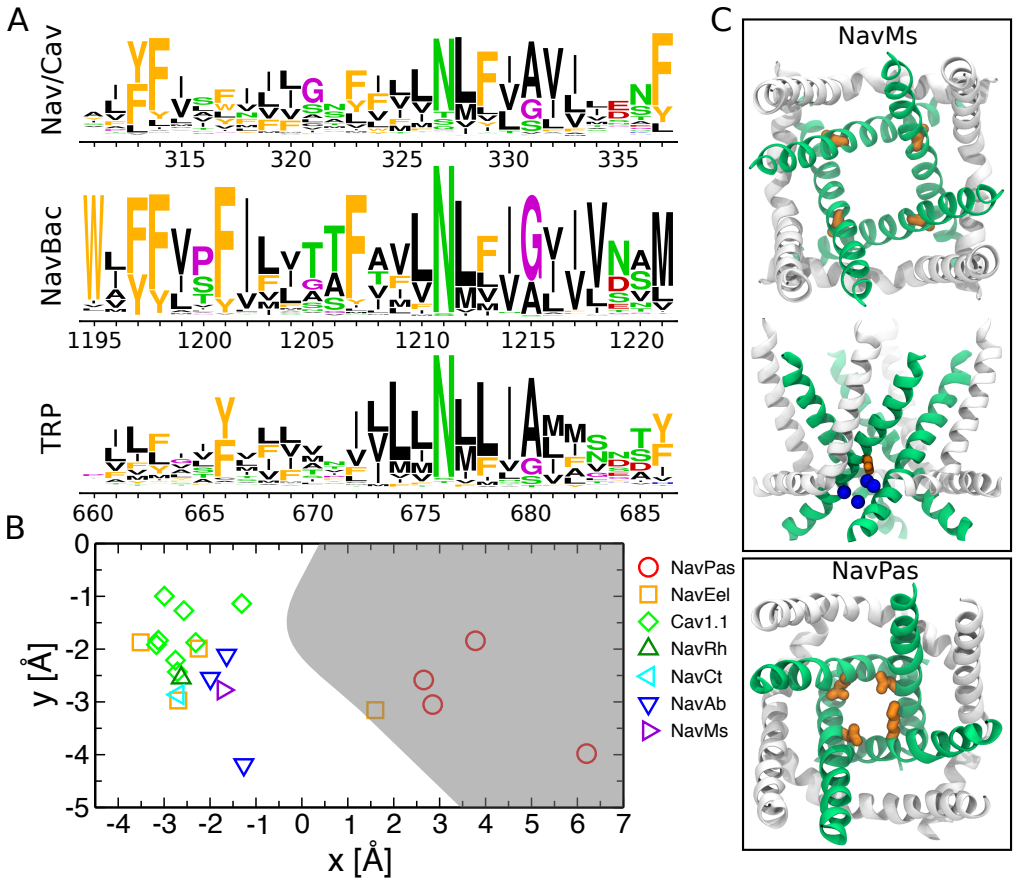

Figure 6: Structurally homologous and evolutionary related families of voltage-gated sodium and calcium channels show a conserved asparagine in S6 and the presence of four hydrated cavities between S6 and S4-S5 linker. A. Multiple sequence alignment of the S6 helix of the eukaryotic voltage-gated sodium and calcium channels (Nav/Cav), bacterial voltage-gated sodium channels (NavBac), and TRP channels (TRP) (12, 40). B. Orientation of the conserved asparagine with respect to the pore in different Nav and Cav structures (28–37). The position of the asparagine side chain in the plane perpendicular to the pore axis is shown. The x-axis is aligned with the vector connecting the Cα-atom of the asparagine and the center of the pore. The pore region is shown in grey. C. The cartoon representation of NavMs (top panel, top and side views are shown) and NavPas (28, 37). The conserved asparagine (shown in orange) is inside the pore in NavPas, and outside of it in NavMs. In NavMs, the water molecules inside the cavity located between the S6 helix and the S4-S5 linker are shown in blue.

The two other lines of evidence lending credibility to our hypothesis come from the alanine-scanning mutagenesis of the S6 residues performed by Susankova et al. (38) and the site-directed mutagenesis of S4-S5 linker residues performed by us in this study. Susankova et al. have identified a clear periodic pattern of the functional effects of mutations, which is consistent with the α-helical structure of S6 (38). Subsequently obtained cryo-EM structures of TRPV1 showed that the residues whose mutation has the most significant effect on activation are located outside of the pore and line the surface of peripheral cavities (Fig. 7). Importantly, the response of the corresponding mutants to capsaicin, voltage and heat was significantly reduced, indicating stabilization of the closed state versus the open one. A possible interpretation for these data is that

the substitution of hydrophobic residues (I672, L673, L674, L678 and M682) with a less hydrophobic one (alanine) promotes the hydration of peripheral cavities and thus stabilizes the closed state.

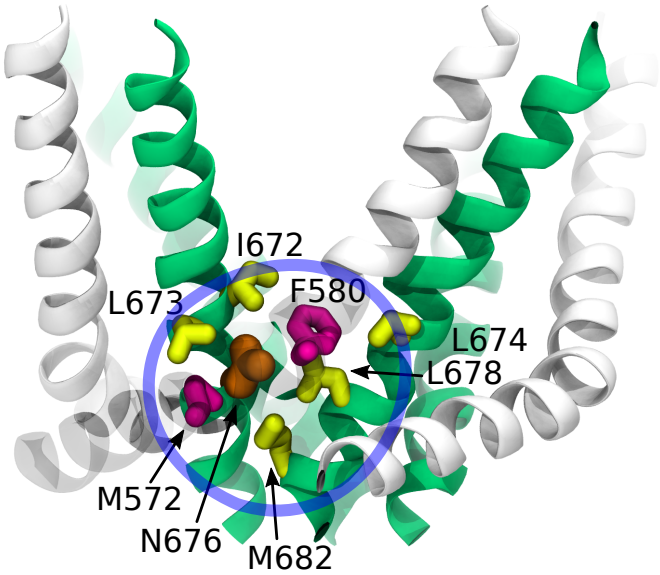

Figure 7: Mutagenesis of residues lining peripheral cavities. S6 residues mutated by Susankova et al. are shown in yellow (38), the S4-S5 linker residues mutated in this study are shown in magenta. The conserved asparagine is represented in orange. The S6 helices and the rest of the pore domain are shown in green and white, respectively. The peripheral cavity is highlighted with a blue circle.

Finally, we sought to further validate our hypothesis and, in line with the experiments by Susankova et al., we performed mutagenesis of two S4-S5 linker residues lining the peripheral cavities: M572 and F580 (Fig. 7). In case of M572, we generated an alanine mutant. In the other case, we chose to increase the polarity at 580 position with minimal structural perturbation; thus we mutated the phenylalanine to tyrosine. Using two-electrode voltage clamp (TEVC) and Ca^{2+} imaging experiments, we characterized the response of the wild type (WT) channel and of the mutants to capsaicin, low pH and heat (Fig. 8). Our results show that F580Y is less sensitive to capsaicin compared to the WT channels in TEVC experiments (Fig. 8A). Since F580 is located far from the vanilloid binding site, it is unlikely that this mutation impairs capsaicin binding. Furthermore, both mutants, M572A and F580Y, showed reduced sensitivity to low pH (Fig. 8B); in the second case, the current was only observed at pH 4 but not at lower proton concentrations. Finally, our results suggest an impaired mechanism of heat-induced activation in both M572A and F580Y (Fig. 8C): for these mutants, the Ca^{2+} responses induced by high temperature were significantly smaller than for the WT; this effect was especially prominent for F580Y. Ca^{2+} responses induced by pH 4 were similar to WT for both mutants (Fig. 8C). Consistent with our TEVC experiments (Fig. 8A), Ca^{2+} responses to capsaicin were reduced in F580Y, but intact in M572A (Fig. 8C). To avoid saturation of the dye by high Ca^{2+} levels induced by capsaicin (41), we used a low affinity Fura-2 derivative Ca^{2+} indicator for these

experiments. While Ca^{2+} responses are not linear readouts of channel activity, the robust reduction of heat-induced Ca^{2+} signals in both mutants compared to intact capsaicin responses for the M572A mutant and intact low pH response for both mutants give a clear indication of impaired heat sensitivity. Overall these experiments show that substitution of M572 and F580 with a more hydrophilic residue results in stabilization of the closed state and therefore they agree with the suggested molecular mechanism for TRPV1 activation.

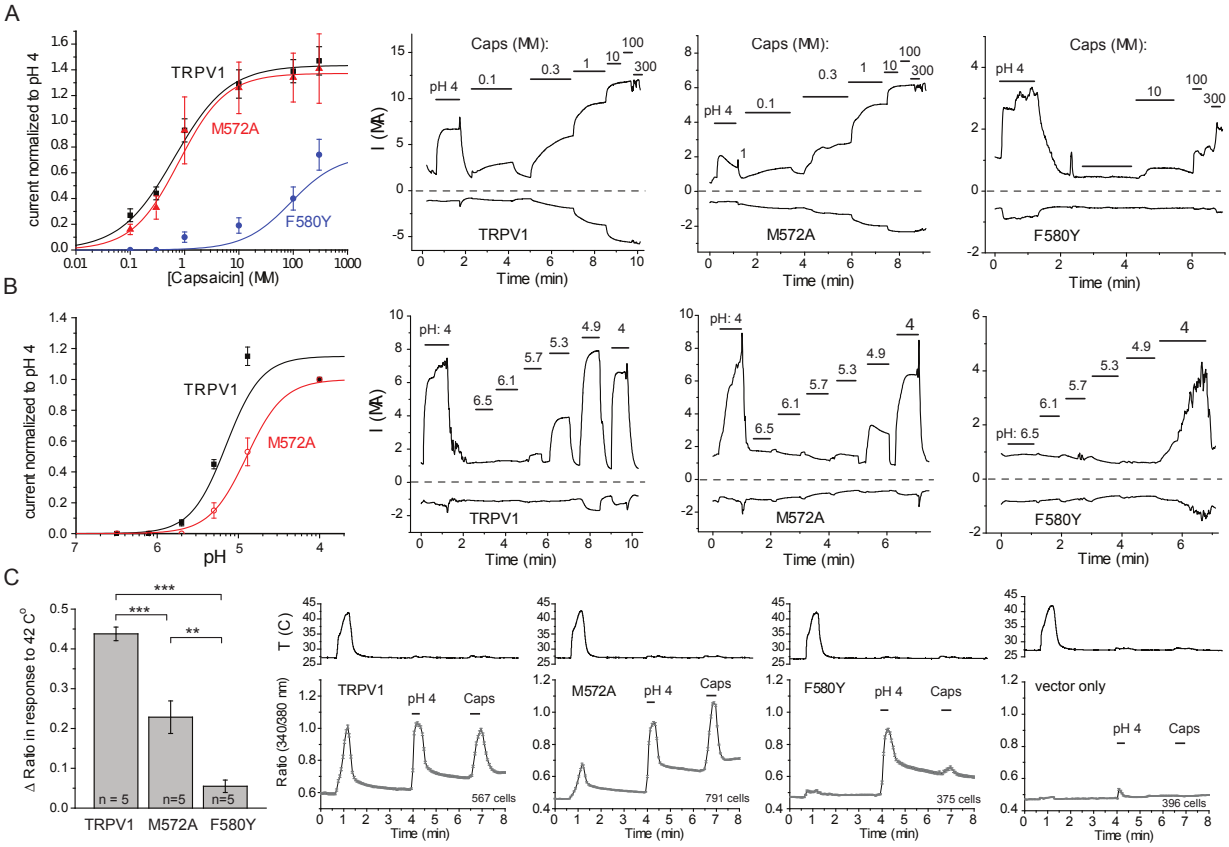

Figure 8: Mutation of the S4-S5 linker residues lining peripheral cavities affects TRPV1 activation by capsaicin, low pH and heat. A. Activation of the wild type (WT), M572A and F580Y by capsaicin: Hill fits of the WT and the mutants' responses to different capsaicin concentrations at 100 mV (currents were normalized to that evoked by pH 4); representative current traces of the WT and the mutants' in response to different capsaicin concentrations are shown on the right. Two-electrode voltage clamp (TEVC) oocyte electrophysiology was performed as described in Methods. Currents at 100 mV and -100 mV are shown. Zero current is indicated by the dashed-line. Oocytes expressing the WT or the mutants were stimulated first with a pH 4 solution and then with successive concentrations of capsaicin. B. Activation of the WT, M572A and F580Y by low pH: Hill fits of the WT and M572A responses to solutions with different proton concentrations (currents were normalized to that evoked by pH 4); representative current traces of the WT, M572A and F580Y in response to low extracellular pH are shown on the right. C. Activation of the WT, M572A and F580Y by heat: statistical summary of the response to heat. The average responses of cells from each coverslip were treated as individual data points; n corresponds to the number of coverslips; statistical significance was calculated with one-way ANOVA, and Bonferoni post hoc comparison. Intracellular Ca^{2+} responses to heat, pH 4 and 0.5

μM capsaicin of the WT, M572A, F580Y and HEK cells transfected with an empty vector are shown on the right. The channels were first stimulated with a heat pulse, followed by the application of a pH 4 solution and capsaicin (0.5 μM). Intracellular Ca^{2+} concentration was measured with low affinity Fura-2 as described in Methods. The traces show average +/- S.E.M. of cells from 5 coverslips (the number of cells is indicated in each panel). Top panel shows average temperatures in the vicinity of cells measured during the experiments using a temperature probe and the pClamp software.

CONCLUSIONS

Despite two decades of extensive investigations, the molecular mechanism of TRPV1 activation is only partially understood. Catching an ion channel in the act of gating is, in general, a complex task requiring techniques with both high temporal and high spatial resolution. NMR spectroscopy and fluorescence/luminescence based approaches are typically the tools of choice but they cannot easily probe the motions of an ion channel when embedded in a cell membrane. This limitation is particularly severe in the case of TRPV1 whose activity shows exquisite dependency on numerous environmental factors, such as lipid composition (8, 41–45), extracellular concentration of Na^{+} (11) and the presence of cholesterol or other fatty acids (46–49). Accordingly, advanced experimental techniques, such as cell unroofing (50, 51) and incorporation of novel unnatural amino acids (26, 51), are being constantly developed to overcome these limitations and introduce only minimal perturbations to the native environment of the channel. Despite the great progress, these techniques have focused so far only on specific aspects of TRPV1 activation. A global picture of this molecular process is still lacking and it is unlikely that a single experimental technique will provide it in the foreseeable future.

Here, prompted by our previous molecular dynamics simulations (10) and bioinformatics analyses (12), we propose a molecular mechanism of activation, which is consistent with previously published data and reconciles seemingly contradictory experimental observations. More than definite answers, our contribution provides testable predictions and an overall framework to rationalize a wealth of existing experimental data. Indeed, despite the novel site-directed mutagenesis experiments presented here, our model is still in part speculative. There are few important limitations in our approach that is worth mentioning. First, our computational investigation focused mostly on the capsaicin-bound state, even though TRPV1 can be activated by heat also in absence of capsaicin. Independent simulations starting from the apo state could assess the robustness of our calculation and thus provide further support to our hypothesis. Second, our site-directed mutagenesis study targeted only two residues. Although consistent with the proposed model, these data are not sufficient to exclude alternative explanations.

Further research will be required to validate the molecular mechanism proposed here. In particular, discriminative experiments, which exclude multiple interpretations, should be designed. For instance, incorporating unnatural amino acids in TRPV1 could

allow for a fine tuning of the polar properties of the pore and the peripheral cavities without perturbing too much their geometry. The same approach could be used to investigate the coupling between the upper and lower gates. According to our model, this involves the interaction between the side chain of N676 and the S6 helix backbone groups. The latter could be modified by introducing appropriately designed unnatural amino acids. From the computational point of view, long unbiased simulations could be used to sample gating events and provide direct confirmation of the activation mechanism. The Anton 2 supercomputer developed by D. E. Shaw Research (52, 53) and available through the Pittsburgh Supercomputing Center provides the opportunity to reach timescales comparable to those required for TRPV1 activation and thus to test the hypothesized chain of molecular events. These simulations ought to involve, ideally, both the apo and the capsaicin-bound states.

In closing, it is interesting to comment on an intriguing possibility emerging from our analyses: we found that the key structural features supporting our hypothesized mechanism are present also in the evolutionary related families of voltage-gated sodium and calcium channels. In particular, the conserved asparagine in the S6 helix, the π-bulge and the peripheral cavities are seemingly conserved beyond the family of TRP channels. This raises the possibility that voltage-gated sodium and calcium channels might share with TRP channels important aspects of the activation mechanism. Future investigations ought to establish whether or not this is the case.

MATERIALS AND METHODS

Molecular dynamics simulations

The molecular dynamics trajectories of the capsaicin-bound closed and open states were taken from our previous study (10). Briefly, the structure of the TRPV1 capsaicin-bound state (7) with four capsaicin molecules (54) was embedded in a hydrated 1-palmitoyl-2-oleoylphosphatidylcholine, POPC, bilayer and surrounded by 150 mM NaCl solution. From 4 to 6 water molecules were added inside each peripheral cavity in one case (this system further relaxed to the closed state), while these cavities were left empty in the other case (this system further relaxed to the open state) (10). The CHARMM36 force field (55) was used for the protein and the POPC lipids, the parameters derived in (54) were used for capsaicin, and the TIP3P model (56) was used for water molecules. The molecular dynamics simulations were performed following a multistep protocol (for the details, see (10)) using NAMD 2.10 (57). The pressure and temperature were kept constant at 1 atm and 300 K, respectively, using Langevin dynamics. A cutoff of 11 Å with a switching function between 8 and 11 Å was used for the vdW interactions. A cutoff of 11 Å was considered for the short-range component of electrostatic interactions, and the long-range component was computed using Particle Mesh Ewald (58). The overall length of the molecular dynamics trajectory for each state was 750 ns. In addition, we performed the molecular dynamics

simulations of the TRPV1 apo state (54) using an analogous setup. The overall length of the molecular dynamics trajectory for this state was 200 ns.

Analysis of sequence conservation

The multiple sequence alignments of the TRP and voltage-gated sodium and calcium channels were taken from our previous studies (12, 40). To analyze the sequence conservation for these families we computed the Shannon entropy profile using the logos website (59).

Estimation of the accessibility of S6 residues to the intracellular solution

To estimate the accessibility of S6 residues to the intracellular solution, we considered the second halves of the molecular dynamics trajectories. We separated the intracellular solution from the rest applying the following procedure. We first calculated the three-dimensional map of water occupancy using the Volmap tool of VMD (60). Based on this we generated a binary map by setting each voxel to either 0 or 1 depending on whether or not the local value of water occupancy overcomes a predefined threshold. After that we used gmx cluster of Gromacs 5.0.4 (61) to group the voxels. This allowed us to identify the cluster containing the intracellular solution and all the regions connected to it. Finally, as a measure of accessibility, we calculated the overlap between the occupancy of the intracellular solution and that of each S6 residue.

Experimental mutagenesis

Xenopus oocyte preparation and electrophysiology. Oocytes from female Xenopus *laevis* frogs were prepared using collagenase digestion as described in (49). Briefly, oocytes were digested using 0.2 mg/ml collagenase (Sigma) in a solution containing 82.5 mM NaCl, 2 mM KCl, 1 mM $MgCl_2$, and 5 mM HEPES, pH 7.4 (OR2) overnight for ~ 16 h at 18 °C in a temperature controlled incubator. Oocytes were selected and kept in OR2 solution supplemented with 1.8 mM $CaCl_2$ and 1% penicillin/streptomycin (Mediatech) at 18 °C. Point mutants of TRPV1 in the pGEMS oocyte vector were generated using the QuikChange kit (Agilent Technologies). cRNA was generated from linearized cDNA using the mMessage mMachine kit (Ambion). cRNA (50 ng) was microinjected into each oocyte using a nanoliter injector system (World Precision Instruments). The experiments were performed 5 days after injection.

Two-electrode voltage clamp (TEVC) measurements were performed as described in (49) in a solution containing 97 mM NaCl, 2 mM KCl, 1 mM $MgCl_2$, 5 mM 2-(N-Morpholino)ethanesulfonic acid (MES) and 5 mM HEPES, pH 7.4. MES was added to our usual extracellular oocyte buffer to be able to set the pH to 4 with HCl in the stimulating solution. Currents were recorded with thin-wall inner filament-containing glass pipettes (World Precision Instruments) filled with 3 M KCl in 1% agarose. Currents were measured with a ramp protocol from -100 to 100 mV performed once 0.5 second from a holding potential of 0 mV, and the currents at -100, 0 and 100 mV were plotted.

Cell culture and Ca^{2+} imaging. Human embryonic kidney 293 (HEK293) cells were obtained from the ATCC and were cultured in minimal essential medium (MEM)

(Invitrogen) containing supplements of 10% (v/v) Hyclone-characterized Fetal Bovine Serum (FBS) (Thermo Scientific), 100 IU/ml penicillin, and 100 µg/ml streptomycin. Transient transfection was performed at ~ 70% cell confluence with the Effectene reagent (QIAGEN) according to the manufacturer's protocol. Cells were incubated with the lipid-DNA complexes overnight. Then, 24 h post-transfection, cells were trypsinized and replated on poly-l-lysine-coated glass coverslips and incubated for an additional 24 h (in the absence of the transfection reagent) before measurements. Cultured HEK cells were kept in a humidity-controlled tissue-culture incubator maintaining 5% CO_2 at 37 °C.

Ca^{2+} imaging measurements were performed with an Olympus IX-51 inverted microscope equipped with a DeltaRAM excitation light source (Photon Technology International). HEK cells were loaded with 2 µM low affinity Fura-2 AM (Abcam) at 37 °C in MEM – FBS for 45 min before the measurement, and dual-excitation images at 340 and 380 nm were recorded with a Roper Cool-Snap digital CCD camera. The standard extracellular solution used in all experiments contained (in mM): 137 NaCl, 5 KCl, 1 $MgCl_2$, 2 $CaCl_2$, 10 HEPES and 10 glucose, pH 7.4 (adjusted with NaOH). For the low pH solution the composition was modified to 137 NaCl, 5 KCl, 1 $MgCl_2$, 2 $CaCl_2$, 5 HEPES, 5 MES and 10 glucose, pH 4.0 (adjusted with HCl). Low pH and capsaicin solution (stock in EtOH) were applied with a gravity driven whole chamber perfusion system. Heat stimulation was performed with custom made system, and solution temperature was continuously recorded with a thermo probe located in a close proximity to the recording field. Data analysis was performed using the Image Master software (Photon Technology International).

ACKNOWLEDGMENTS

This work was partially supported by National Institutes of Health through grants R01GM093290, S10OD020095, and P01GM055876 and National Science Foundation through grants ACI-1614804 and CNS-1625061.

REFERENCES

1. Caterina MJ, et al. (1997) The capsaicin receptor: a heat-activated ion channel in the pain pathway. *Nature* 389(6653):816–824.

2. Tominaga M, et al. (1998) The cloned capsaicin receptor integrates multiple pain-producing stimuli. *Neuron* 21(3):531–543.

3. Hayes P, et al. (2000) Cloning and functional expression of a human orthologue of rat vanilloid receptor-1. *Pain* 88(2):205–215.

4. Julius D, Basbaum AI (2001) Molecular mechanisms of nociception. *Nature* 413(6852):203–210.

5. Carnevale V, Rohacs T (2016) TRPV1: A Target for Rational Drug Design. *Pharm Basel Switz* 9(3). doi:10.3390/ph9030052.

6. Liao M, Cao E, Julius D, Cheng Y (2013) Structure of the TRPV1 ion channel determined by electron cryo-microscopy. *Nature* 504(7478):107–112.

7. Cao E, Liao M, Cheng Y, Julius D (2013) TRPV1 structures in distinct conformations reveal activation mechanisms. *Nature* 504(7478):113–118.

8. Gao Y, Cao E, Julius D, Cheng Y (2016) TRPV1 structures in nanodiscs reveal mechanisms of ligand and lipid action. *Nature* 534(7607):347–351.

9. Yang F, et al. (2015) Structural mechanism underlying capsaicin binding and activation of the TRPV1 ion channel. *Nat Chem Biol* 11(7):518–524.

10. Kasimova MA, et al. (2018) Ion Channel Sensing: Are Fluctuations the Crux of the Matter? *J Phys Chem Lett* 9(6):1260–1264.

11. Jara-Oseguera A, Bae C, Swartz KJ (2016) An external sodium ion binding site controls allosteric gating in TRPV1 channels. *eLife* 5. doi:10.7554/eLife.13356.

12. Palovcak E, Delemotte L, Klein ML, Carnevale V (2015) Comparative sequence analysis suggests a conserved gating mechanism for TRP channels. *J Gen Physiol* 146(1):37–50.

13. McGoldrick LL, et al. (2018) Opening of the human epithelial calcium channel TRPV6. *Nature* 553(7687):233–237.

14. Paulsen CE, Armache J-P, Gao Y, Cheng Y, Julius D (2015) Structure of the TRPA1 ion channel suggests regulatory mechanisms. *Nature* 520(7548):511–517.

15. Winkler PA, Huang Y, Sun W, Du J, Lü W (2017) Electron cryo-microscopy structure of a human TRPM4 channel. *Nature* 552(7684):200–204.

16. Autzen HE, et al. (2017) Structure of the human TRPM4 ion channel in a lipid nanodisc. *Science*:eaar4510.

17. Guo J, et al. (2017) Structures of the calcium-activated, non-selective cation channel TRPM4. *Nature* 552(7684):205–209.

18. Shen PS, et al. (2016) The Structure of the Polycystic Kidney Disease Channel PKD2 in Lipid Nanodiscs. *Cell* 167(3):763-773.e11.

19. Grieben M, et al. (2017) Structure of the polycystic kidney disease TRP channel Polycystin-2 (PC2). *Nat Struct Mol Biol* 24(2):114–122.

20. Wilkes M, et al. (2017) Molecular insights into lipid-assisted Ca(2+) regulation of the TRP channel Polycystin-2. *Nat Struct Mol Biol* 24(2):123–130.

21. Saotome K, Singh AK, Yelshanskaya MV, Sobolevsky AI (2016) Crystal structure of the epithelial calcium channel TRPV6. *Nature* 534(7608):506–511.

22. Zubcevic L, et al. (2016) Cryo-electron microscopy structure of the TRPV2 ion channel. *Nat Struct Mol Biol* 23(2):180–186.

23. Huynh KW, et al. (2016) Structure of the full-length TRPV2 channel by cryo-EM. *Nat Commun* 7:11130.

24. Hughes TET, et al. (2018) Structural basis of TRPV5 channel inhibition by econazole revealed by cryo-EM. *Nat Struct Mol Biol* 25(1):53–60.

25. Yin Y, et al. (2018) Structure of the cold- and menthol-sensing ion channel TRPM8. *Science* 359(6372):237–241.

26. Steinberg X, et al. (2017) Conformational dynamics in TRPV1 channels reported by an encoded coumarin amino acid. *eLife* 6:e28626.

27. Salazar H, et al. (2009) Structural determinants of gating in the TRPV1 channel. *Nat Struct Mol Biol* 16(7):704–710.

28. Shen H, et al. (2017) Structure of a eukaryotic voltage-gated sodium channel at near-atomic resolution. *Science* 355(6328). doi:10.1126/science.aal4326.

29. Yan Z, et al. (2017) Structure of the Nav1.4-β1 Complex from Electric Eel. *Cell* 170(3):470-482.e11.

30. Wu J, et al. (2016) Structure of the voltage-gated calcium channel Ca(v)1.1 at 3.6 Å resolution. *Nature* 537(7619):191–196.

31. Wu J, et al. (2015) Structure of the voltage-gated calcium channel Cav1.1 complex. *Science* 350(6267):aad2395.

32. Zhang X, et al. (2012) Crystal structure of an orthologue of the NaChBac voltage-gated sodium channel. *Nature* 486:130–134.

33. Tsai C-J, et al. (2013) Two Alternative Conformations of a Voltage-Gated Sodium Channel. *J Mol Biol* 425(22):4074–4088.

34. Payandeh J, Scheuer T, Zheng N, Catterall WA (2011) The crystal structure of a voltage-gated sodium channel. *Nature* 475(7356):353–358.

35. Payandeh J, Gamal El-Din TM, Scheuer T, Zheng N, Catterall WA (2012) Crystal structure of a voltage-gated sodium channel in two potentially inactivated states. *Nature* 486:135–139.

36. Lenaeus MJ, et al. (2017) Structures of closed and open states of a voltage-gated sodium channel. *Proc Natl Acad Sci U S A* 114(15):E3051–E3060.

37. Sula A, et al. (2017) The complete structure of an activated open sodium channel. *Nat Commun* 8:14205.

38. Susankova K, Ettrich R, Vyklicky L, Teisinger J, Vlachova V (2007) Contribution of the putative inner-pore region to the gating of the transient receptor potential vanilloid subtype 1 channel (TRPV1). *J Neurosci Off J Soc Neurosci* 27(28):7578–7585.

39. O'Reilly AO, et al. (2017) Mutagenesis of the NaChBac sodium channel discloses a functional role for a conserved S6 asparagine. *Eur Biophys J* 46(7):665–674.

40. Kasimova MA, Granata D, Carnevale V (2016) Chapter Nine-Voltage-Gated Sodium Channels: Evolutionary History and Distinctive Sequence Features. *Curr Top Membr* 78:261–286.

41. Lukacs V, Rives J-M, Sun X, Zakharian E, Rohacs T (2013) Promiscuous Activation of Transient Receptor Potential Vanilloid 1 (TRPV1) Channels by Negatively Charged Intracellular Lipids. *J Biol Chem* 288(49):35003–35013.

42. Poblete H, et al. (2015) Molecular determinants of phosphatidylinositol 4,5-bisphosphate (PI(4,5)P2) binding to transient receptor potential V1 (TRPV1) channels. *J Biol Chem* 290(4):2086–2098.

43. Chuang HH, et al. (2001) Bradykinin and nerve growth factor release the capsaicin receptor from PtdIns(4,5)P2-mediated inhibition. *Nature* 411(6840):957–962.

44. Cao E, Cordero-Morales JF, Liu B, Qin F, Julius D (2013) TRPV1 channels are intrinsically heat sensitive and negatively regulated by phosphoinositide lipids. *Neuron* 77(4):667–679.

45. Rohacs T (2015) Phosphoinositide regulation of TRPV1 revisited. *Pflugers Arch* 467(9):1851–1869.

46. Liu M, Huang W, Wu D, Priestley JV (2006) TRPV1, but not P2X3, requires cholesterol for its function and membrane expression in rat nociceptors. *Eur J Neurosci* 24(1):1–6.

47. Matta JA, Miyares RL, Ahern GP (2007) TRPV1 is a novel target for omega-3 polyunsaturated fatty acids. *J Physiol* 578(Pt 2):397–411.

48. Picazo-Juárez G, et al. (2011) Identification of a binding motif in the S5 helix that confers cholesterol sensitivity to the TRPV1 ion channel. *J Biol Chem* 286(28):24966–24976.

49. Morales-Lázaro SL, et al. (2016) Inhibition of TRPV1 channels by a naturally occurring omega-9 fatty acid reduces pain and itch. *Nat Commun* 7:13092.

50. Gordon SE, Senning EN, Aman TK, Zagotta WN (2016) Transition metal ion FRET to measure short-range distances at the intracellular surface of the plasma membrane. *J Gen Physiol* 147(2):189–200.

51. Zagotta WN, Gordon MT, Senning EN, Munari MA, Gordon SE (2016) Measuring distances between TRPV1 and the plasma membrane using a noncanonical amino acid and transition metal ion FRET. *J Gen Physiol* 147(2):201–216.

52. Shaw DE, et al. (2009) Millisecond-scale Molecular Dynamics Simulations on Anton. *Proceedings of the Conference on High Performance Computing Networking, Storage and Analysis*, SC '09. (ACM, New York, NY, USA), pp 39:1–39:11.

53. Shaw DE, et al. (2014) Anton 2: Raising the Bar for Performance and Programmability in a Special-Purpose Molecular Dynamics Supercomputer. *SC14: International Conference for High Performance Computing, Networking, Storage and Analysis*, pp 41–53.

54. Elokely K, et al. (2016) Understanding TRPV1 activation by ligands: Insights from the binding modes of capsaicin and resiniferatoxin. *Proc Natl Acad Sci U S A* 113(2):E137-145.

55. Mackerell AD Jr, Feig M, Brooks CL 3rd (2004) Extending the treatment of backbone energetics in protein force fields: limitations of gas-phase quantum

mechanics in reproducing protein conformational distributions in molecular dynamics simulations. *J Comput Chem* 25(11):1400–1415.

56. Jorgensen WL, Chandrasekhar J, Madura JD, Impey RW, Klein ML (1983) Comparison of simple potential functions for simulating liquid water. *J Chem Phys* 79(2):926.

57. Phillips JC, et al. (2005) Scalable molecular dynamics with NAMD. *J Comput Chem* 26(16):1781–1802.

58. Darden T, York D, Pedersen L (1993) Particle mesh Ewald: An N·log(N) method for Ewald sums in large systems. *J Chem Phys* 98(12):10089–10092.

59. Crooks GE, Hon G, Chandonia J-M, Brenner SE (2004) WebLogo: a sequence logo generator. *Genome Res* 14(6):1188–1190.

60. Humphrey W, Dalke A, Schulten K (1996) VMD: Visual molecular dynamics. *J Mol Graph* 14(1):33–38.

61. Abraham MJ, et al. (2015) GROMACS: High performance molecular simulations through multi-level parallelism from laptops to supercomputers. *SoftwareX* 1–2:19–25.